Effect of carbonate additive on the microstructure and corrosion resistance of plasma electrolytic oxidation coating on Mg–9Li–3Al alloy

Siyuan Jin[1], *Xiaochun Ma*[1], *Ruizhi Wu*[1,3),✉], *Tingqu Li*[2),✉], *Jiaxiu Wang*[1], *Boris L Krit*[4], *Legan Hou*[4], *Jinghuai Zhang*[1], *and Guixiang Wang*[1]

1) Key Laboratory of Superlight Materials & Surface Technology, Ministry of Education, Harbin Engineering University, Harbin 150001, China

2) College of Materials Science and Engineering, Jilin Institute of Chemical Technology, Jilin 132022, China

3) College of Science, Heihe University, Heihe 164300, China

4) Moscow Aviation Institute, National Research University, Moscow 125993, Russia

Abstract: Carbonate was added to the silicate system electrolyte to improve the corrosion resistance of the plasma electrolytic oxidation coating on Mg–9Li–3Al (wt%, LA93) alloy. The influences of carbonate on the morphology, structure, and phase composition of the coating were investigated by scanning electron microscopy, energy dispersive spectrometry, X-ray diffraction, and X-ray photoelectron spectroscopy. The corrosion resistance of the coating was evaluated by electrochemical experiment, hydrogen evolution, and immersion test. The results showed that the addition of carbonate resulted in a denser coating with increased hardness, and the corrosion-resistant Li_2CO_3 phase was formed. Electrochemical experiments showed that compared with the coating without carbonate, the corrosion potential of the carbonate coating positively shifted (24 mV), and the corrosion current density was reduced by approximately an order of magnitude. The coating with carbonate addition possessed a high corrosion resistance and long-term protection capability.

Keywords: Mg–Li alloy; plasma electrolytic oxidation; corrosion resistance; carbonate

1. Introduction

As the lightest engineering material, Mg–Li alloy has the advantages of low density, high specific strength and specific stiffness, and excellent electromagnetic shielding performance [1]. This alloy is widely used in the fields of aerospace, weapon, 3C (computer, communication, consumer electronic), and so on [2]. However, the relatively low potential of magnesium (−2.34 V) and high chemical activity of lithium lead to the poor corrosion resistance of Mg–Li alloys and severely limit their wide-range applications [3–4]. At present, the improvement of the corrosion resistance of alloys is mainly divided into two aspects. One is alloying or processing, in which the corrosion resistance improvement is limited [5–6]. On the other hand, the corrosion resistance of alloys can be greatly improved through surface treatment technology, including chemical conversion [7], sol–gel [8], electroplating [9], and anodization [10], etc. Plasma electrolytic oxidation (PEO) technology has attracted wide attention due to its simple process, environmentally friendly electrolyte, high hardness, and excellent bonding force of the coating [11–12].

The composition of electrolytes influences the morphology and corrosion resistance of the PEO coating. At present, the main electrolytes for magnesium alloys include silicate, phosphate, meta-aluminate, etc. The various additives in electrolytes can adjust the microstructure, phase composition, thickness, and corrosion resistance of coatings. In the PEO process for AZ91D alloy, the additives K_2ZrF_6 and ethylene-dinitrilotetraacetic acid disodium salt dihydrate (EDTA-NA) in the alkaline phosphoric acid solution have evident effects on the coating [13]. The addition of K_2ZrF_6 slightly increases the thickness of the coating and generates a thermally stable phase ZrO_2, which improves the corrosion resistance. After the addition of EDTA-NA, the thickness of the coating is almost unchanged, but the breakdown voltage is effectively reduced. As a result, the pore size of the coating is reduced, and the corrosion resistance is significantly improved. In the PEO process for Mg–8.5Li alloy, the addition of phosphate generates an insoluble $Mg_3(PO_4)_2·22H_2O$ on the coating to cover the micro-pores and discharge channels, thereby slowing the attack on the coating by corrosive media [14]. The addition of Ce causes the formation of CeO in the PEO coating of Mg–Y–Zn alloy, thereby blocking the micro-pores and cracks and improving the corrosion resistance greatly [15]. The addition of Na_2WO_4 in the electrolyte can also improve the corrosion resistance of the PEO coating on Mg–14Li alloy, and this result can be ascribed to the denser coating and

Springer

1454

Int. J. Miner. Metall. Mater., Vol. 29, No. 7, Jul. 2022

the formation of more corrosion-resistant and thermally stable Mg_2SiO_4 and WO_3 phases [16]. The addition of carbonate to the electrolyte system in the PEO process of AZ31 alloy can be used to adjust the microstructure of the coating and reduce the pore size. However, no new phases will be formed. Moreover, the influence of the addition of carbonate on the corrosion resistance of the coating has not been studied in detail [17].

From the recent literature, many reports show that Li can easily react with CO_2 in the air on the surface of Mg–Li alloys, which generates a corrosion-resistant Li_2CO_3 phase and improves the corrosion resistance of Mg–Li alloys [18–22]. Based on the information mentioned above, researchers proposed whether the addition of carbonate in the electrolyte for the PEO coating of Mg–Li alloys will cause the formation of the Li_2CO_3 phase in the coating and whether it will cause changes in the coating microstructure and improvement of corrosion resistance. Under this motivation, 5 g/L sodium carbonate was added to the alkaline sodium silicate electrolyte in this study, and the ceramic coating was prepared on the surface of the LA93 alloy by the PEO process. The influences of the addition of carbonate on the microstructure and corrosion resistance of the coating were investigated.

2. Experimental

2.1. Preparation of PEO coating

The LA93 alloy (9wt% Li, 3wt% Al, and the rest were Mg) was used as the experimental sample with dimensions of 20 mm × 20 mm × 4 mm. The samples were mechanically ground up to 2000 grit with SiC papers, cleaned in ethanol, and dried in air for the subsequent PEO process.

The composition of the electrolyte was 10 g/L Na_2SiO_3, 4 g/L KF, and 2 g/L NaOH in distilled water, without (marked as A) and with (marked as B) 5 g/L Na_2CO_3. In the previous exploratory experiments, the increase in the concentration of carbonate had a certain effect on the porosity and pore size of the coating. When the carbonate concentration was extremely high, the small pores gradually connected together to form larger defects, and finally, the optimal concentration of 5 g/L Na_2CO_3 was selected. In the PEO process, the stainless steel and the working sample were used as the cathode and anode, respectively. A cooling system was used to maintain the electrolyte at a temperature of 15–20°C. The DC double-pulse power was used as the experimental power supply, and a constant current mode was adopted. The PEO duration was 10 min with a fixed current density of 5 A/dm², duty cycle of 50%, and frequency of 600 Hz. The PEO-processed samples were cleaned with distilled water and air dried for subsequent characterizations.

2.2. Coating characterization and corrosion performance test

Field-emission scanning electron microscopy (FE-SEM) combined with an energy dispersive spectrometry (EDS) system was employed to observe the coating morphology and measure the chemical composition of the samples. Image Pro Plus 6.0 software was used to calculate the coating porosity. At least five different positions in the SEM image were measured to ensure accuracy. X-ray diffraction (XRD) with Cu K_α radiation was used for phase component analysis in the scan range of 20°–80° at a speed of 2°/min. The microhardness of the coating was measured by a hardness tester (HXS-1000Z), and the loading force and time were 1.96 N and 15 s, respectively. To ensure the exactness, we measured 10 points at different positions of each sample and used their average value. The surface chemistry of samples was analyzed by X-ray photoelectron spectroscopy (XPS). Al K_α radiation from a monochromatic X-ray source and a 500 µm light spot size was used. The binding energies were corrected by setting the C 1s peak at 284.8 eV.

The electrochemical test was carried out in 0.1 M NaCl solution in an electrochemical workstation (Zahner IM6). A three-electrode cell was used in the electrochemical test, with saturated calomel as a reference electrode, the samples as the working electrode (area of 1 cm²), and the platinum electrode as the counter electrode. The polarization curve was measured at the scanning speed of 2 mV/s. After the test, Corrview software was used to fit the polarization curve with Tafel mode. For the electrochemical impedance spectra (EIS) test, the frequency range was set to 100 kHz to 100 mHz, and the disturbance signal was 10 mV. All tests were carried out at room temperature, and each test was carried out thrice to ensure repeatability and accuracy. ZView software was used to fit the EIS data. Chi-squared values were required to be less than 10^{-3} to ensure the accurate fitting of the results.

The samples were immersed in 0.1 M NaCl solution to further investigate the long-term corrosion resistance. The immersion test was carried out for a maximum of 168 h, and the solution was changed every 24 h. In addition, the samples were subjected to hydrogen evolution experiments for 168 h in 0.1 M NaCl solution at room temperature.

3. Results and discussion

3.1. Morphological characterization of the PEO coating

Fig. 1 shows the morphology of the PEO coating of LA93 alloy with and without Na_2CO_3. Both the prepared coatings exhibited a typical PEO coating morphology, with a number of pores and microcracks. In the PEO process, the molten oxide was ejected through the discharge channel under the action of the electric spark, met the relatively cold electrolyte on the surface of the sample, and rapidly solidified [23–25]. The comparison of Fig. 1(b) and (d) with Fig. 1(a) and (c) revealed that the addition of carbonate significantly reduced the pore size and microcracks, but the porosity increased (Table 1). Although the introduction of an appropriate amount of carbonate caused a small increase in the porosity (5.2% to 5.9%), it resulted in an evident reduction of the average pore size from 1.28 to 0.68 µm. Corrosive ions enter easily through large pores, thus attacking and damaging the coating. Therefore, the reduction of pore size is favorable for the cor-
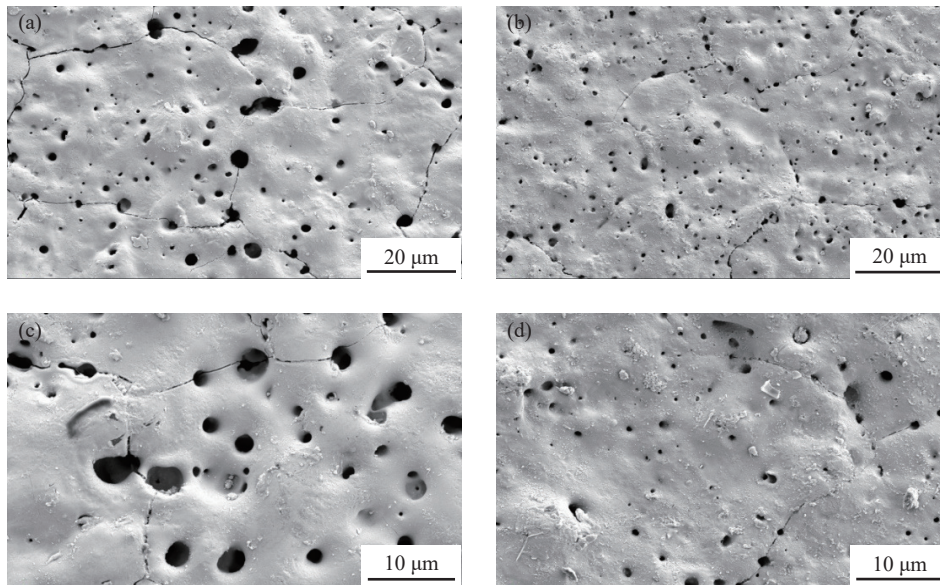
Fig. 1.   SEM images of the surface morphology of PEO coatings without (a, c) and with (b, d) Na$_2$CO$_3$.

Table 1.   Average pore size, porosity, microhardness, and thickness of coatings without and with Na$_2$CO$_3$

Sample	Average pore size / μm	Porosity / %	Microhardness, HV	Thickness / μm
LA93 alloy	—	—	58	—
Without Na$_2$CO$_3$	1.28	5.2	208	20.25
With Na$_2$CO$_3$	0.68	5.9	387	22.74

rosion resistance of the coating. Simultaneously, the addition of carbonate improves the conductivity of the electrolyte and reduces the breakdown voltage in the PEO process. The final voltage was reduced from 410 to 330 V. The discharge effect becomes weaker, and the number of large pores generated during the breakdown process is reduced, resulting in a dense coating [17].

Fig. 2 shows the element mappings of the PEO coatings without and with Na$_2$CO$_3$. The chemical composition of the PEO coatings without and with carbonate mainly consisted of Mg, Si, O, and Na; and Mg, Si, O, Na, and C, respectively. Mg originated from the substrate, whereas Si, O, Na, and C came from the electrolyte solution. Coating A had no C added before and after the reaction, but C appeared in the spectrum. In Section 3.2, the occurrence of C without carbonate coating is discussed in detail. Fig. 2 shows that the addition of carbonate significantly increased the carbon content on the surface. From the cross-sectional view and element distribution diagram of coatings A and B in Fig. 3, both coatings consisted of inner and outer layers [26]. Numerous pores and cracks, which were generated by electric spark discharge and gas overflow during the coating formation, can be found in the outer layer of coating A. Meanwhile, the inner layer was relatively denser. Compared with coating A, coating B was denser and had fewer defects. In addition, as shown in Table 1, the thicknesses of coatings A and B were 20.25 and 20.74 μm, respectively. Both coatings had a thickness of more than 20 μm to ensure that the indentation depth cannot cross the interface between the PEO coating and LA93 alloy during the hardness test. The microhardness of coating B (HV 387)

increased by 86.7% compared with coating A (HV 208) and by 567.2% compared with LA93 alloy (HV 58). In summary, the results prove that the carbonate additive in the PEO process can significantly increase the microhardness of the coating, and the coating becomes more uniform and denser and contains fewer defects.

3.2. Composition of the PEO coating

Fig. 4 shows the XRD patterns of LA93 alloy and the PEO coating without and with Na$_2$CO$_3$. The large bulge at 20°–30° should be an amorphous phase, which is probably caused by the rapid solidification of the molten oxide ejected from the discharge channel onto the coating [27]. The LA93 base alloy was composed of α-Mg and β-Li phases, whereas coatings A and B mainly consisted of MgO, Mg$_2$SiO$_4$, α-Mg, and β-Li phases. The appearance of α-Mg and β-Li is due to the porous structure of the coating and X-ray penetration of the pores to reach the substrate. The peak intensities of α-Mg and β-Li in coating B were significantly weakened, which can confirm that coating B is denser than coating A. In addition, the peak of Li$_2$CO$_3$ was found in coating B, which may be explained by the diffusion of Li under the action of the electric spark in the PEO process and its reaction with carbonate in the electrolyte to generate Li$_2$CO$_3$ in the coating, as shown in Eq. (1), consistent with other studies [21–22,28]. In addition, the formation of Mg$_2$CO$_3$ was not found in the XRD pattern because Mg^{2+} in the solution is mainly consumed by SiO$_3^{2-}$ to form the thermodynamically stable forsterite phase [29–30]. Given that the charge of Mg is larger than that of Li, it has a lower thermal decomposition temperature [31].
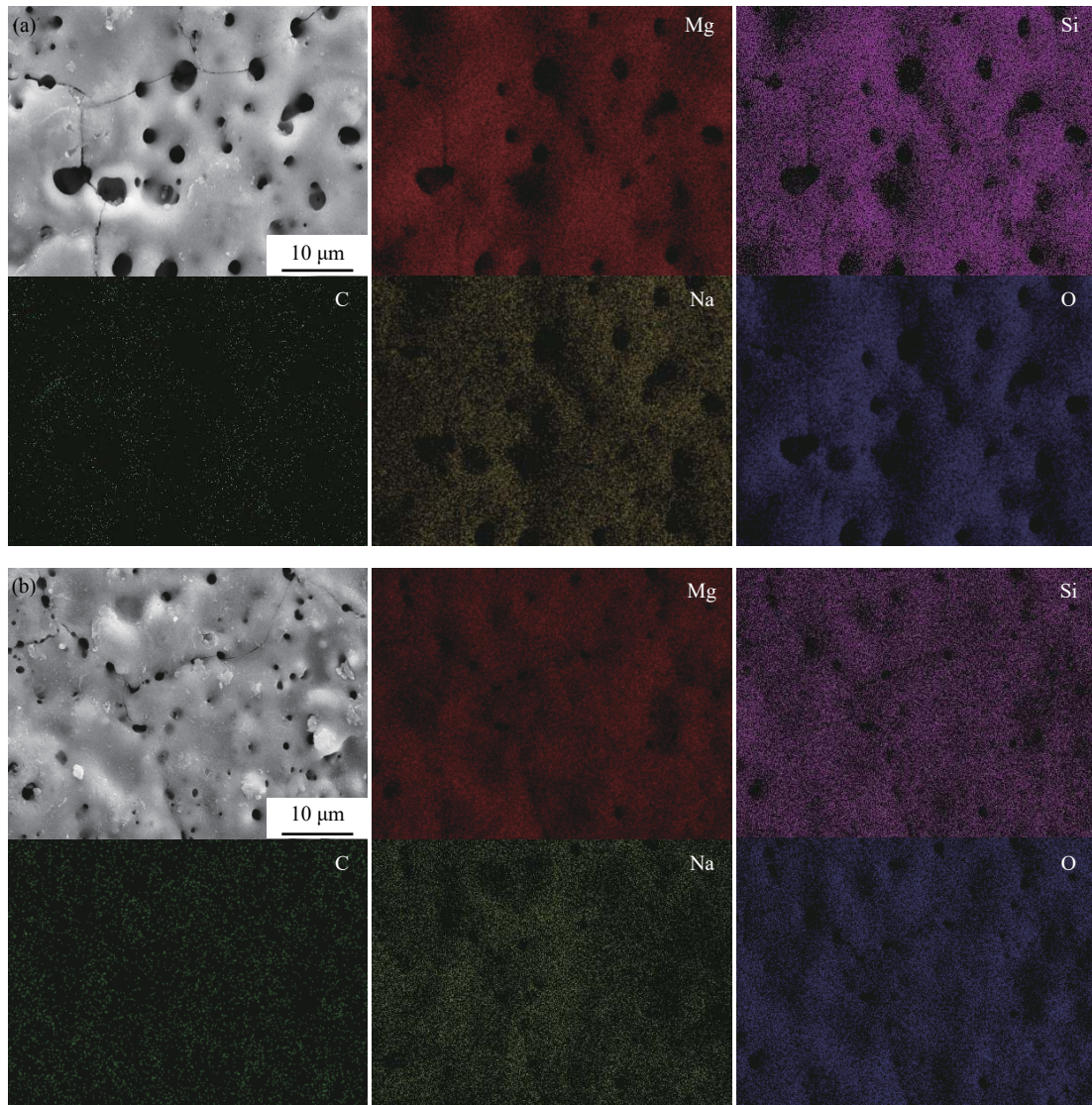
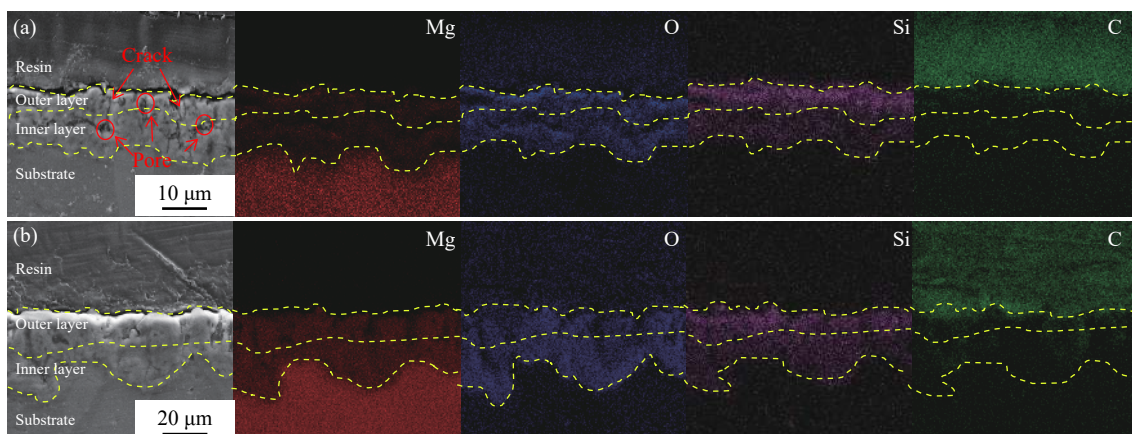**Fig. 2.   Element mappings of PEO coatings without (a) and with (b) Na$_2$CO$_3$.**

Fig. 3.   SEM images of cross-sectional of PEO coatings without (a) and with (b) Na$_2$CO$_3$.

$$2Li^+ + CO_3^{2-} \rightarrow Li_2CO_3 \tag{1}$$

The chemical composition of coatings A and B was measured by XPS (Fig. 5). The Mg 1s spectrum was composed of the diffraction peaks of Mg$_2$SiO$_4$ (1304.5 eV), MgO (1304 eV), and Mg(OH)$_2$ (1303.2 eV) obtained by fitting [32]. The composition of the diffraction peaks in the Si 2p spectrum

corresponded to γ-Mg$_2$SiO$_4$ (103 eV) and α-Mg$_2$SiO$_4$ (102.1 eV) [14,33]. The diffraction peaks in the Li 1s spectrum of coating A corresponded to Li$_2$CO$_3$ (55.2 eV), LiOH (54.9 eV), and Li (56.4 eV). The composition of the diffraction peaks in the Li 1s spectrum in coating B corresponded to Li$_2$CO$_3$ (55.2 eV) and LiOH (54.9 eV) [5]. The diffraction

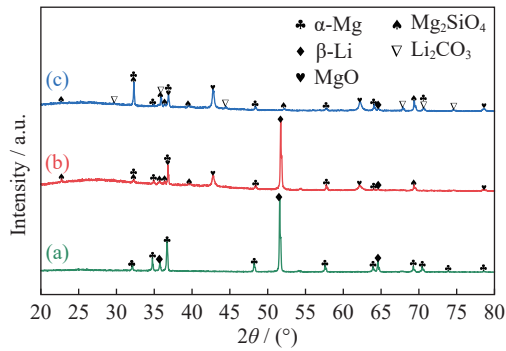**Fig. 4.** XRD patterns of (a) LA93 alloy and PEO coatings without (b) and with (c) Na_2CO_3.

peak of Li_2CO_3 appeared in the spectrum of coating A, which is consistent with the EDS result. Thus, the presence of carbonate in coating A can be ascribed to CO_2 pollution in the air [34–35]. In the PEO process, the electric spark discharge causes the CO_2 in the air to be ionized and incorporated into the coating formation reaction, as shown in the reactions in Eqs. (2)–(3) [34]. However, its content was low and could not be detected in XRD.
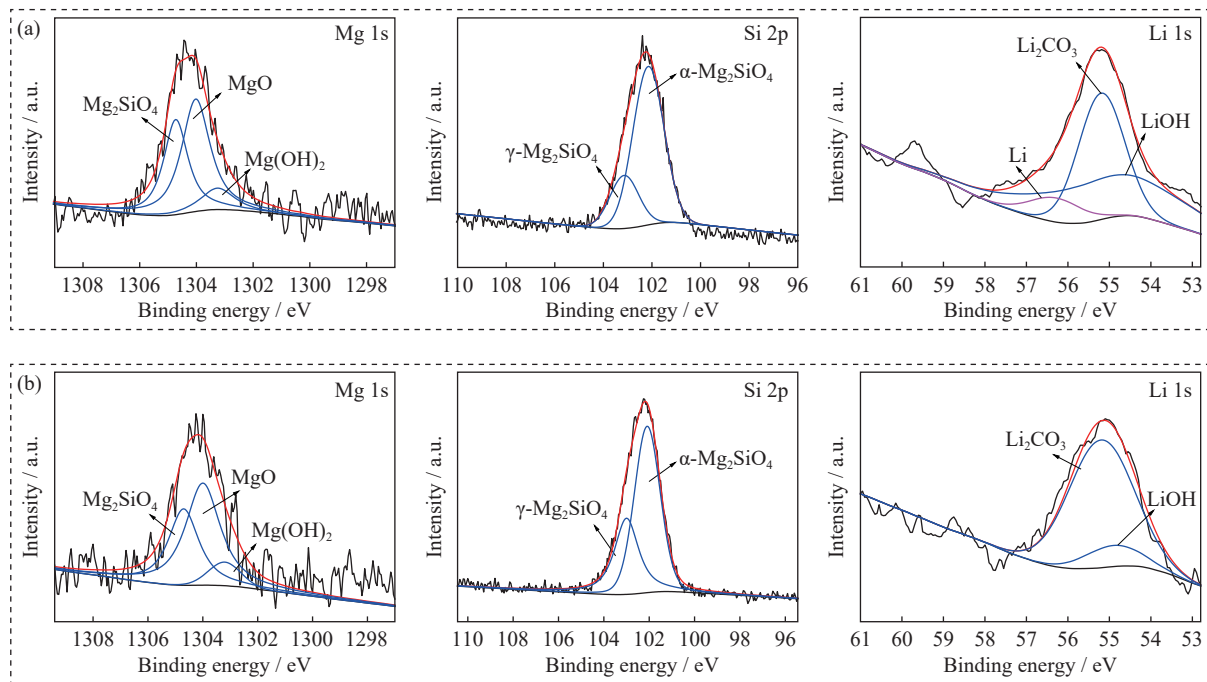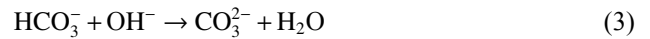
$$2CO_2 + H_2O \rightarrow HCO_3^- + H^+ \tag{2}$$

$$HCO_3^- + OH^- \rightarrow CO_3^{2-} + H_2O \tag{3}$$

Fig. 5. XPS spectra of PEO coating without (a) and with (b) Na_2CO_3.

3.3. Evaluation of corrosion resistance

3.3.1. Electrochemical characterization

Fig. 6 and Table 2 show the polarization curves and the fitting results of the LA93 alloy and PEO coatings without and with Na_2CO_3. After PEO treatment, the corrosion potential positively shifted, and the corrosion current was reduced by 2–3 orders of magnitude. The findings indicate that the corrosion resistance of the sample after PEO treatment is improved greatly. Furthermore, compared with coating A, the addition of carbonate caused the positive shifting of the corrosion potential of coating B, and the corrosion current was reduced by about an order of magnitude. These results indicate that the addition of carbonate to the electrolyte results in a significant improvement in the corrosion resistance of the coating.

Fig. 7 displays the EIS curves of the LA93 alloy and the PEO coatings without and with Na_2CO_3. In the low-frequency impedance modulus $|Z|$ shown in Fig. 7(b), the $|Z|$ values of coatings A and B were notably larger than that of

LA93 alloy, which shows that their corrosion resistance has been greatly improved. The $|Z|$ of coating B was slightly higher than that of coating A. This finding reveals that the ad-
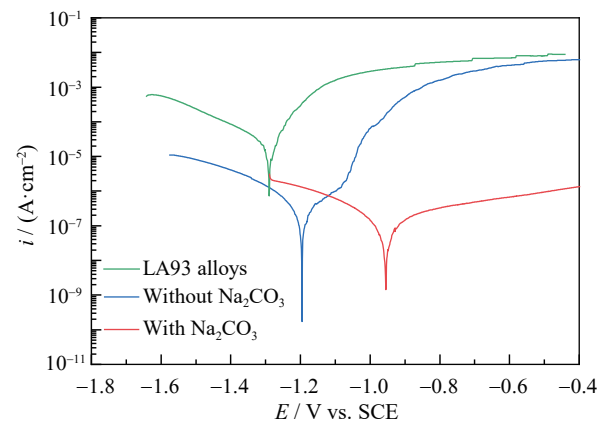

Fig. 6. Polarization curves of the LA93 alloy and PEO coatings without and with Na_2CO_3. SCE represents saturated calomel electrode.

Table 2.   Fitting results of polarization tests of the LA93 alloy and PEO coatings without and with Na$_2$CO$_3$

| Sample	E_{corr} / V vs. SCE	I_{corr} / (A·cm^{-2})
LA93	−1.29	2.7391×10^{-5}
Without Na$_2$CO$_3$	−1.195	7.4597×10^{-7}
With Na$_2$CO$_3$	−0.955	9.6257×10^{-8}

dition of carbonate can be used to adjust well the coating structure to increase its corrosion resistance [30]. Fig. 7(b) and (c) shows that the Bode plots of coatings A and B were relatively similar. Thus, although the addition of carbonate causes the formation of the Li$_2$CO$_3$ phase and a compact coating structure, the cross-sectional view reveals that the coating is still composed of a loose outer film layer and a dense inner film layer. Therefore, these coatings still show a relatively similar corrosion process [23,33]. From the Nyquist plot shown in Fig 7(a), LA93 alloy included a high-frequency capacitive loop and low-frequency inductive loop, and coatings A and B were composed of capacitive loops. The diameter of the capacitive loops reflects the corrosion resistance, and the appearance of the low-frequency inductive loops means that the sample dissolved and pitted corrosion [36]. LA93 alloy had an inductive loop in the low-frequency region due to the high chemical activities of magnesium and lithium. However, no inductive loop was present in coatings A and B at low frequencies, indicating that the coatings protect the substrate well from the attack of corrosive ions.

The EIS plots of LA93 alloy, coating A, and coating B were fitted to further analyze the corrosion resistance of the coating. Fig. 8 and Table 3 show the equivalent circuit and its fitting results. In the equivalent circuit, R_s is the solution resistance, and R_{ct} and CPE$_{dl}$ represent the charge transfer resistance and double-layer capacitance, respectively. R_{out} is the resistance of the outer layer, and CPE$_{out}$ represents the constant phase element of the outer layer. R_{in} represents the resistance of the inner layer, and CPE$_{in}$ represents the constant phase element of the inner layer. R_L and L are resistance and inductance components in the low-frequency range, respectively. The phase angle plot in Fig. 7(c) shows that coatings A and B are different from LA93 alloy and has at least two time constants. The peaks of the PEO coating in the high- and low-frequency regions correspond to the loose outer layer and the dense inner layer, respectively, consistent with those observed in the cross-sectional view. The results of fitting in Table 3 show that the impedance of the outer layer of coating A is approximately 1/13 of the impedance of the inner layer. The impedance of the outer film layer of coating B is approximately 1/30 of the impedance of the inner film layer. Thus, the corrosion resistance of the inner layer is significantly higher than that of the outer layer. Moreover, the addition of carbonate increases the resistance of the outer film layer from 2843 to 3427 Ω·cm^2, whereas the resistance of the inner film layer increases from 36315 to 104250 Ω·cm^2, an increase of 2.8 times. The EIS curve and the fitting results also confirmed that the addition of carbonate can improve the corro-

sion resistance of the coating.

3.3.2. Hydrogen evolution and immersion test

Hydrogen evolution and immersion test for a maximum of 168 h were carried out to better understand the corrosion behavior of the coating, and EIS was used to study the corrosion behavior of coatings A and B. Fig. 9 shows the hydrogen evolution of LA93 alloy and the PEO coatings without and with Na$_2$CO$_3$ in 0.1 M NaCl solution for 168 h. The volume of hydrogen evolved gradually increased with time. The hydrogen evolution rate of the LA93 alloy increased significantly at the initial stage of the immersion and then rose
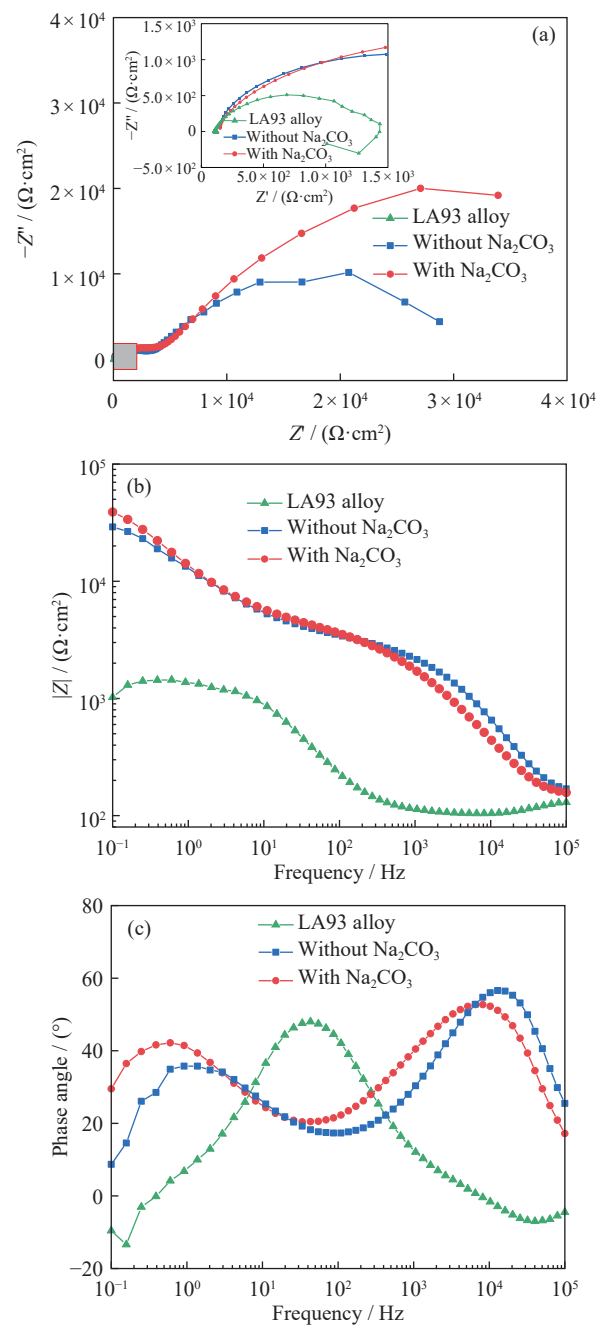
Fig. 7.   EIS plots for the LA93 alloy and PEO coatings without and with Na$_2$CO$_3$: (a) Nyquist plots, and the insert is the partial enlarged detail of the square area; (b, c) Bode plots of impedance and phase angle versus frequency.
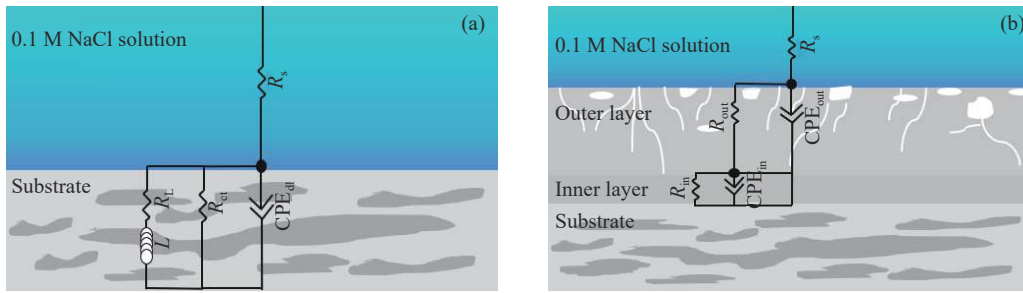
Fig. 8. Equivalent circuits for fitting of the impedance data of (a) the LA93 alloy and (b) PEO coatings without and with Na_2CO_3.

Table 3.   EIS fitting results for the LA93 alloy and PEO coatings without and with Na_2CO_3 in 0.1 M NaCl solution

Sample	R_s / ($\Omega \cdot cm^2$)	CPE_{dl} / ($\Omega^{-1} \cdot cm^{-2} \cdot s^n$)	n_{dl}	R_{ct} / ($\Omega \cdot cm^2$)	R_L / ($\Omega \cdot cm^2$)	L / ($H \cdot cm^2$)
LA93	110	2.3624×10^{-5}	0.85769	1291	1972	4744

Sample	R_s / ($\Omega \cdot cm^2$)	CPE_{out} / ($\Omega^{-1} \cdot cm^{-2} \cdot s^n$)	n_{out}	R_{out} / ($\Omega \cdot cm^2$)	CPE_{in} / ($\mu\Omega^{-1} \cdot cm^{-2} \cdot s^n$)	n_{in}	R_{in} / ($\Omega \cdot cm^2$)
Without Na_2CO_3	121.6	1.3594×10^{-7}	0.84935	2843	2.2936×10^{-5}	0.61763	36315
With Na_2CO_3	121	4.1868×10^{-7}	0.79035	3427	2.6477×10^{-5}	0.60061	104250

Note: n is the angular frequency, and $0 < n < 1$; if $n = 1$, CPE is the pure capacitance; if $n = 0$, CPE is the pure resistance.

steadily and slowly. The main reason is that the corrosion products of LA93 alloy form a thin film layer on the surface, playing a certain protective role. However, the film layer is extremely thin to provide sufficient protection, resulting in corrosion again. The hydrogen evolution volume of the sample was significantly reduced after the PEO treatment. From the macroscopic morphology, pitting corrosion appeared on the surface of the sample without carbonate at 32 h. The surface of the sample with carbonate showed pitting corrosion at 96 h. This result proves that the addition of carbonate can effectively improve the long-term protection of the coating.

Fig. 10 shows the EIS plot of coatings A and B immersed in 0.1 M NaCl solution for different times. Coating A at 1 h immersion had a similar-sized capacitance loop compared with that without immersion. The diameter of the capacitive loop of the coating gradually decreased when the immersion time was between 6–24 h. When the immersion time reached 72 h, the capacitive loop became smaller, and an inductance

Fig. 9.   Hydrogen evolution data for LA93 alloy and PEO coatings without and with Na_2CO_3 in 0.1 M NaCl solution for 168 h.

loop appeared at low frequencies, which means that corrosion occurs on the coating surface. Eventually, the capacitive loop reached a minimal value at 168 h. By contrast, coating B showed a similar capacitive loop diameter at 1 and 6 h immersion in comparison with that without immersion, indicating that the coating has excellent stability and corrosion resistance under short periods of immersion. The diameter of the capacitive loop of coating B was slightly reduced at 24 h, indicating that the coating can still attain good protection during the initial immersion. After 72 h of immersion, the diameter of the capacitive loop was further reduced, and no inductive loop appeared. When the immersion time reached 168 h, an inductive loop appeared in the Nyquist plots, which indicates that corrosion occurs.

The impedance of the sample measured at the lowest frequency ($|Z|_{f=0.1\,Hz}$) can be used to evaluate the corrosion resistance of the sample [37]. Fig. 11 shows that the slope of reduction was similar for coatings A and B at 1–6 h immersion, indicating that the coating has a similar corrosion rate in the early stage of corrosion. This finding also implies that the outer layers of coatings A and B exhibit a similar corrosion mechanism, i.e., Cl⁻ entered through the discharge channel to attack the coating. Coating B maintained a large value of $|Z|_{f=0.1\,Hz}$ (34576 $\Omega \cdot cm^2$) at the immersion time of 24 h, which indicates that it can resist the attack of Cl⁻ better than coating A. The value of $|Z|_{f=0.1\,Hz}$ of coating B was approximately 1.67 times larger than that of coating A when the immersion time reached 72 h. When the immersion time reached 168 h, the $|Z|_{f=0.1\,Hz}$ of coating B (13041 $\Omega \cdot cm^2$) was close to that of coating A (11514 $\Omega \cdot cm^2$). Through hydrogen evolution, coating B had been corroded during the 92 h immersion, and this finding also indicates that the corrosive medium reaches the substrate. Therefore, in the EIS test, its impedance of $|Z|_{f=0.1Hz}$ dropped sharply. Fig. 12 reveals that after 168 h of immersion, the surface of coating A presented local and pitting cor-

1460

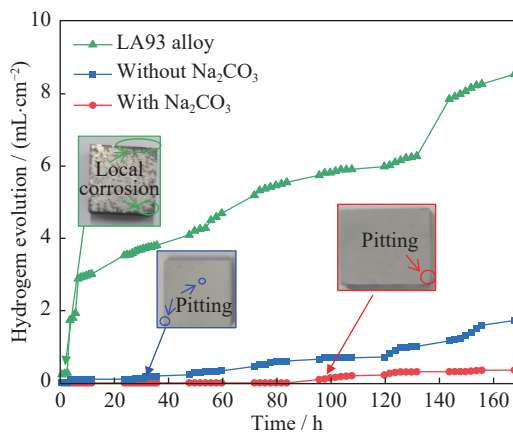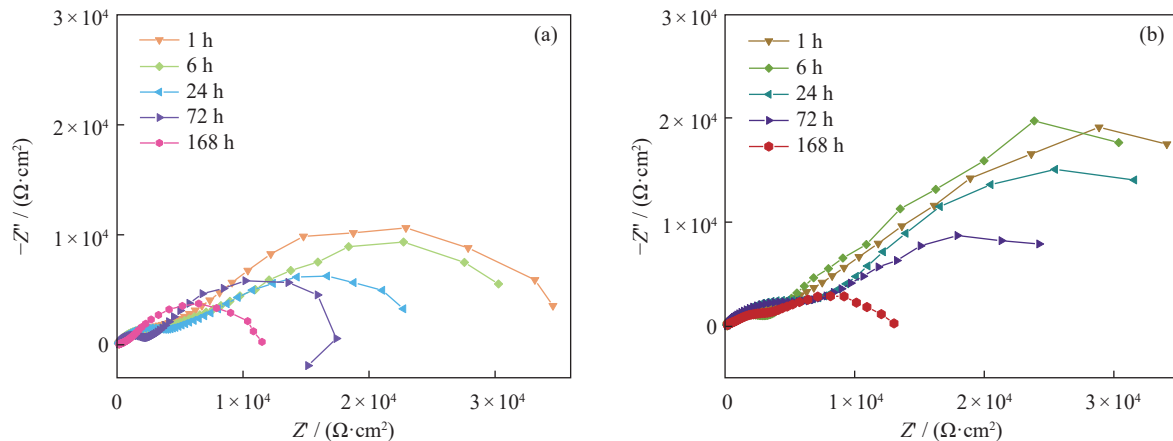*Int. J. Miner. Metall. Mater., Vol. 29, No. 7, Jul. 2022*

Fig. 10. EIS plots of PEO coatings formed in silicate electrolyte without (a) and with (b) Na₂CO₃ during the immersion test.

rosion, whereas coating B exhibited slight pitting corrosion. In addition, although the impedance values of both coatings were relatively close in the EIS test after immersion for 168 h, coating B retained a good protective capability. Moreover, an interesting phenomenon was observed. The corrosion of coatings A and B notably started and expanded from the edge of the sample. Especially, the edge of coating A had localized corrosion. The occurrence of this phenomenon may be caused by the point discharge effect [38]. In the PEO process, the discharge intensity in the edge area is significantly greater than in the central part. Thus, more and larger defects form in the edge area. The addition of carbonate can reduce the breakdown voltage of the coating, thereby weakening the point discharge effect and reducing the number of large pores in the edge area [17,39]. The findings also demonstrate that the modification of the microstructure by the addition of carbonate leads to a more long-period protective capacity of coating B compared to coating A.

According to the diagram of the reaction process of coating formation in silicate electrolyte without and with Na₂CO₃ additive and the corrosion process of coating in 0.1 M NaCl solution in Fig. 13, the addition of carbonate caused the generation of more CO₂ gas in the formation process of coating B. The pore size of the coating was reduced, and the coating became denser and contained fewer defects. This finding mainly resulted from the reaction of carbonate with Mg to

form Mg_2CO_3 during the PEO process, whereas Mg_2CO_3 is thermally decomposed to generate CO_2 gas at high temperatures. The escape of CO_2 gas within the coating left numerous small pores, leading to the increase in porosity, and the reaction equations are shown in Eqs. (4)–(6) [37,40]. In the PEO process, the discharge preferentially accumulates in the large-size defects, and the violent spark discharge causes a large amount of thermal stress in the coating, which increases the size of pores and cracks. By contrast, the increased number of small pores results in a uniform spark discharge, reducing the thermal stress generated during the discharge process. Thus, the large-sized pores significantly reduced, and the porosity increased, which caused the coating to become more uniform, especially in the inner layer. A dense coating can effectively prevent Cl⁻ damage to the coating and corrosion of the substrate through the discharge channel, which can effectively improve the corrosion resistance of the coating. On the other hand, the added carbonate reacted with the Li ions diffusing from the base alloy, causing the formation of a more stable and corrosion-resistant Li_2CO_3. Numerous studies have also proven that the formation of Li_2CO_3 can effectively improve corrosion resistance [19,41]. The excellent corrosion resistance of coating B is mainly due to the modification of its structure and the formation of corrosion-resistant Li_2CO_3 by the addition of carbonate.

$$Mg - 2e \rightarrow Mg^{2+} \tag{4}$$

$$Mg^{2+} + CO_3^{2-} \rightarrow MgCO_3 \tag{5}$$

$$MgCO_3 \rightarrow MgO + CO_2 \uparrow \tag{6}$$

4. Conclusions

Corrosion-resistant ceramic oxide coatings were prepared on the surface of LA93 alloy by the PEO process, and the effect of Na₂CO₃ additive in the electrolyte was investigated. The main conclusions can be drawn as follows.

(1) The addition of 5 g/L Na₂CO₃ to the electrolyte effectively modified the coating microstructure. The pore size of the coating was significantly reduced, and the porosity was increased. Large defects were evidently reduced, and the coating became denser and showed a high microhardness.
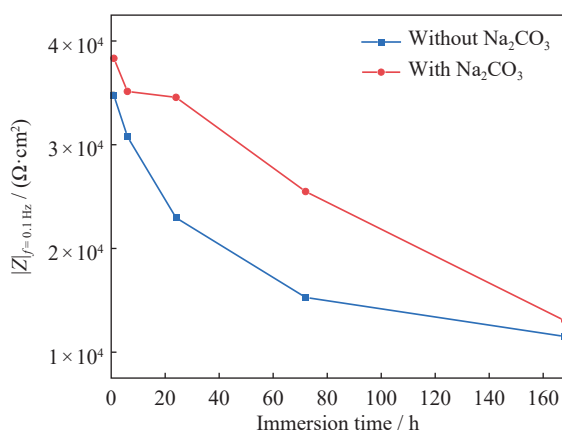

Fig. 11. Corrosion resistance as a function of immersion time of the corresponding PEO coatings.
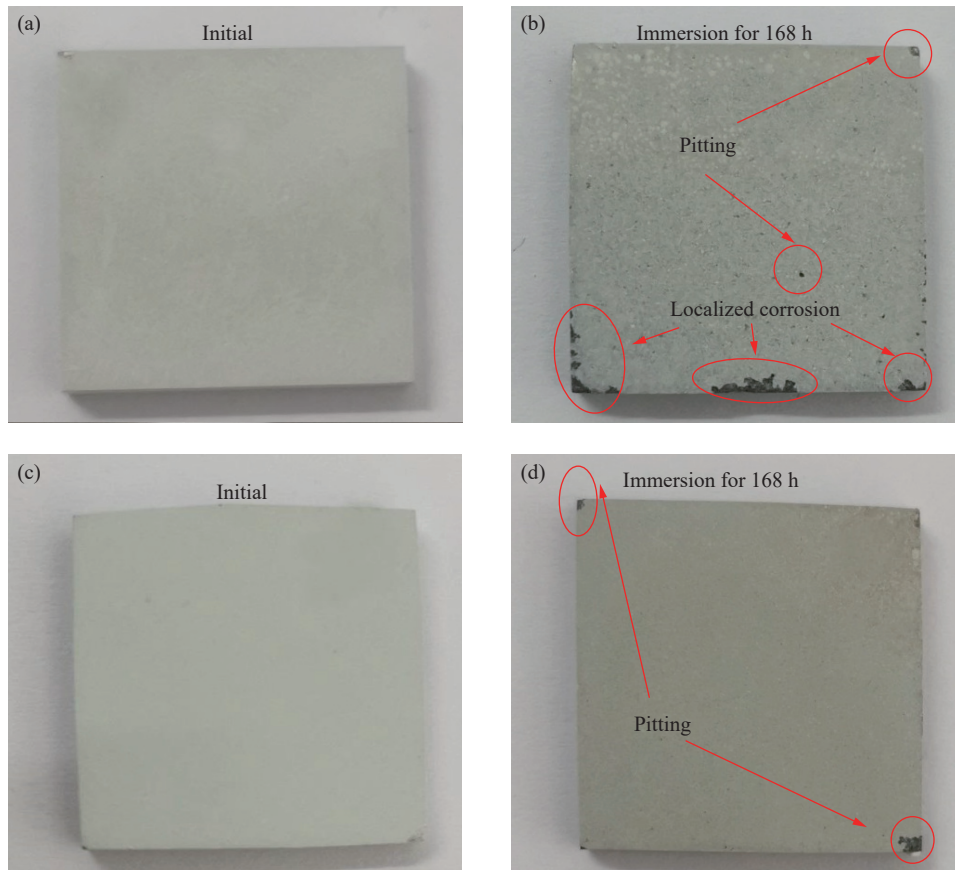
Fig. 12.   Photographs of PEO coatings formed in a silicate electrolyte without (a, b) and with (c, d) Na$_2$CO$_3$ additive immersion test.
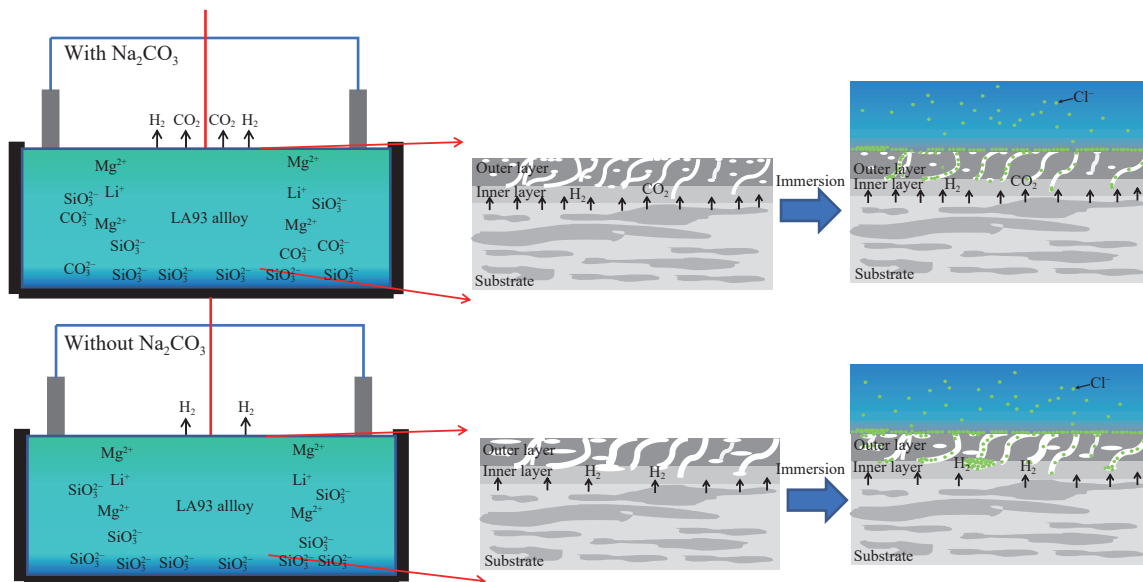

Fig. 13.   Schematic of the working mechanism of the formation of a coating in the silicate electrolyte without and with Na$_2$CO$_3$ additive and coating corrosion process in 0.1 M NaCl solution.

(2) The PEO coatings were mainly composed of MgO and Mg$_2$SiO$_4$. The addition of carbonate caused the coating to generate more stable and corrosion-resistant Li$_2$CO$_3$, which further improved the corrosion resistance of the coating.

(3) The addition of carbonate can effectively improve the corrosion resistance of the coating and can extend the long-term protection capability of the coating.

Acknowledgements

the Open Foundation of Key Laboratory of Superlight Materials & Surface Technology of Ministry of Education, China (No. HEU10202104).

Conflict of Interest

We declare that we have no financial and personal relationships with other people or organizations that can inappropriately influence our work, there is no professional or other personal interest of any nature or kind in any product, service and/or company that could be construed as influencing the position presented in, or the review of, the manuscript entitled.

References

[1] J.H. Wang, L. Xu, R.Z. Wu, D. An, Z. Wei, J.X. Wang, J. Feng, J.H. Zhang, L.G. Hou, and M.D. Liu, Simultaneous achievement of high electromagnetic shielding effectiveness (X-band) and strength in Mg–Li–Zn–Gd/MWCNTs composite, *J. Alloys Compd.*, 882(2021), art. No. 160524.

[2] A. Mehrabi, R. Mahmudi, and H. Miura, Superplasticity in a multi-directionally forged Mg–Li–Zn alloy, *Mater. Sci. Eng. A*, 765(2019), art. No. 138274.

[3] S.Y. Jin, H.Y. Liu, R.Z. Wu, F. Zhong, L.G. Hou, and J.H. Zhang, Combination effects of Yb addition and cryogenic-rolling on microstructure and mechanical properties of LA141 alloy, *Mater. Sci. Eng. A*, 788(2020), art. No. 139611.

[4] J.H. Wang, L. Xu, R.Z. Wu, J. Feng, J.H. Zhang, L.G. Hou, and M.L. Zhang, Enhanced electromagnetic interference shielding in a duplex-phase Mg–9Li–3Al–1Zn alloy processed by accumulative roll bonding, *Acta Metall. Sinica Engl. Lett.*, 33(2020), No. 4, p. 490.

[5] Y.Q. He, C.Q. Peng, Y. Feng, R.C. Wang, and J.F. Zhong, Effects of alloying elements on the microstructure and corrosion behavior of Mg–Li–Al–Y alloys, *J. Alloys Compd.*, 834(2020), art. No. 154344.

[6] D. Orlov, K.D. Ralston, N. Birbilis, and Y. Estrin, Enhanced corrosion resistance of Mg alloy ZK60 after processing by integrated extrusion and equal channel angular pressing, *Acta Mater.*, 59(2011), No. 15, p. 6176.

[7] L.Y. Wang, X.M. Xiao, E.Y. Liu, S.R. Yu, X.L. Yin, J. Wang, G. Zhu, Q. Li, and J. Li, Fabrication of superhydrophobic needle-like Ca–P coating with anti-fouling and anti-corrosion properties on AZ31 magnesium alloy, *Colloids Surf. A*, 620(2021), art. No. 126568.

[8] B.T. da Fonseca, E. D'Elia, J.M. Siqueira Júnior, S.M. Oliveira, K.L. Castro, and E.S. Ribeiro, Study of the characteristics and properties of the SiO$_2$/TiO$_2$/Nb$_2$O$_5$ material obtained by the sol–gel process, *Sci. Rep.*, 11(2021), No. 1, art. No. 1106.

[9] C.A. Huang, C.K. Lin, and Y.H. Yeh, The corrosion and wear resistances of magnesium alloy (LZ91) electroplated with copper and followed by 1 μm-thick chromium deposits, *Thin Solid Films*, 519(2011), No. 15, p. 4774.

[10] J.M. Zhang, K. Wang, X. Duan, Y. Zhang, H. Cai, and Z.H. Wang, Effect of hydrothermal treatment time on microstructure and corrosion behavior of micro-arc oxidation/layered double hydroxide composite coatings on LA103Z Mg–Li alloy in 3.5 wt.% NaCl solution, *J. Mater. Eng. Perform.*, 29(2020), No. 6, p. 4032.

[11] B.Y. Qian, W. Miao, M. Qiu, F. Gao, D.H. Hu, J.F. Sun, R.Z. Wu, B. Krit, and S. Betsofen, Influence of voltage on the corrosion and wear resistance of micro-arc oxidation coating on Mg–8Li–2Ca alloy, *Acta Metall. Sinica Engl. Lett.*, 32(2019),

[12] A. Apelfeld, B. Krit, V. Ludin, N. Morozova, B. Vladimirov, and R.Z. Wu, The characterization of plasma electrolytic oxidation coatings on AZ41 magnesium alloy, *Surf. Coat. Technol.*, 322(2017), p. 127.

[13] L.Y. An, Y. Ma, Y.P. Liu, L. Sun, S. Wang, and Z.Y. Wang, Effects of additives, voltage and their interactions on PEO coatings formed on magnesium alloys, *Surf. Coat. Technol.*, 354(2018), p. 226.

[14] Z.J. Li, Q.H. Ren, X.X. Wang, Q. Kuang, D.B. Ji, R.X. Yuan, and X.Y. Jing, Effect of phosphate additive on the morphology and anti-corrosion performance of plasma electrolytic oxidation coatings on magnesium–lithium alloy, *Corros. Sci.*, 157(2019), p. 295.

[15] M. Mohedano, P. Pérez, E. Matykina, B. Pillado, G. Garcés, and R. Arrabal, PEO coating with Ce-sealing for corrosion protection of LPSO Mg–Y–Zn alloy, *Surf. Coat. Technol.*, 383(2020), art. No. 125253.

[16] Z.J. Li, Y. Yuan, P.P. Sun, and X.Y. Jing, Ceramic coatings of LA141 alloy formed by plasma electrolytic oxidation for corrosion protection, *ACS Appl. Mater. Interfaces*, 3(2011), No. 9, p. 3682.

[17] X.B. Wang, X.B. Tian, C.Z. Gong, and S.Q. Yang, Effect of Na$_2$CO$_3$ on energy consumption of micro-arc oxidation of magnesium alloy, *Rare Met. Mater. Eng.*, 41(2012), No. S1, p. 187.

[18] C.Q. Li, Z.P. Tong, Y.B. He, H.P. Huang, Y. Dong, and P. Zhang, Comparison on corrosion resistance and surface film of pure Mg and Mg–14Li alloy, *Trans. Nonferrous Met. Soc. China*, 30(2020), No. 9, p. 2413.

[19] S. Tang, T.Z. Xin, W.Q. Xu, D. Miskovic, C.Q. Li, N. Birbilis, and M. Ferry, The composition-dependent oxidation film formation in Mg–Li–Al alloys, *Corros. Sci.*, 187(2021), art. No. 109508.

[20] W.Q. Xu, N. Birbilis, G. Sha, Y. Wang, J.E. Daniels, Y. Xiao, and M. Ferry, A high-specific-strength and corrosion-resistant magnesium alloy, *Nat. Mater.*, 14(2015), No. 12, p. 1229.

[21] Y. Yan, Y. Qiu, O. Gharbi, N. Birbilis, and P.N.H. Nakashima, Characterisation of Li in the surface film of a corrosion resistant Mg–Li(–Al–Y–Zr) alloy, *Appl. Surf. Sci.*, 494(2019), p. 1066.

[22] C.Q. Li, Y.B. He, and H.P. Huang, Effect of lithium content on the mechanical and corrosion behaviors of HCP binary Mg–Li alloys, *J. Magnes. Alloys*, 9(2021), No. 2, p. 569.

[23] J.J. Yang, X.P. Lu, C. Blawert, S.C. Di, and M.L. Zheludkevich, Microstructure and corrosion behavior of Ca/P coatings prepared on magnesium by plasma electrolytic oxidation, *Surf. Coat. Technol.*, 319(2017), p. 359.

[24] H.P. Duan, K.Q. Du, C.W. Yan, and F.H. Wang, Electrochemical corrosion behavior of composite coatings of sealed MAO film on magnesium alloy AZ91D, *Electrochim. Acta*, 51(2006), No. 14, p. 2898.

[25] B. Yin, Z.J. Peng, J. Liang, K.J. Jin, S.Y. Zhu, J. Yang, and Z.H. Qiao, Tribological behavior and mechanism of self-lubricating wear-resistant composite coatings fabricated by one-step plasma electrolytic oxidation, *Tribol. Int.*, 97(2016), p. 97.

[26] J. da Silva Rodrigues, L. Marasca Antonini, A.A. da Cunha Bastos, J. Zhou, and C. de Fraga Malfatti, Corrosion resistance and tribological behavior of ZK30 magnesium alloy coated by plasma electrolytic oxidation, *Surf. Coat. Technol.*, 410(2021), art. No. 126983.

[27] E. Wierzbicka, B. Vaghefinazari, S.V. Lamaka, M.L. Zheludkevich, M. Mohedano, L. Moreno, P. Visser, A. Rodriguez, J. Velasco, R. Arrabal, and E. Matykina, Flash-PEO as an alternative to chromate conversion coatings for corrosion protection of Mg alloy, *Corros. Sci.*, 180(2021), art. No. 109189.

[28] Q.X. Xia, D.J. Zhang, D.Q. Li, Z.H. Jiang, and Z.P. Yao, Preparation of the plasma electrolytic oxidation coating on Mg–Li

alloy and its thermal control performance, *Surf. Coat. Technol.*, 369(2019), p. 252.

[29] L. Liu, S.R. Yu, E.Y. Liu, Y. Zhao, B.Y. Wang, Y.F. Niu, K. Zhang, G. Zhu, and Q. Li, Preparation and characterization of micro-arc oxidation coating on hollow glass microspheres/Mg alloy degradable composite, *Mater. Chem. Phys.*, 271(2021), art. No. 124935.

[30] X.B. Wang, X.B. Tian, C.Z. Gong, and S.Q. Yang, Na_2CO_3-induced gas evolution reaction and morphology modulation on magnesium alloy during micro-arc oxidation, *J. Inorg. Mater.*, 26(2011), No. 7, p. 721.

[31] C.Y. Chang, S.Y. Yang, and J.C.C. Chan, Solubility product of amorphous magnesium carbonate, *J. Chin. Chem. Soc.*, 68(2021), No. 3, p. 476.

[32] L. Wang, T. Shinohara, and B.P. Zhang, XPS study of the surface chemistry on AZ31 and AZ91 magnesium alloys in dilute NaCl solution, *Appl. Surf. Sci.*, 256(2010), No. 20, p. 5807.

[33] K. Qian, W.Z. Li, X.P. Lu, X.X. Han, Y. Jin, T. Zhang, and F.H. Wang, Effect of phosphate-based sealing treatment on the corrosion performance of a PEO coated AZ91D Mg alloy, *J. Magnes. Alloys*, 8(2020), No. 4, p. 1328.

[34] A. Pardo, S. Merino, M.C. Merino, I. Barroso, M. Mohedano, R. Arrabal, and F. Viejo, Corrosion behaviour of silicon–carbide-particle reinforced AZ92 magnesium alloy, *Corros. Sci.*, 51(2009), No. 4, p. 841.

[35] H.B. Yao, Y. Li, and A.T.S. Wee, Passivity behavior of melt-spun Mg–Y Alloys, *Electrochim. Acta*, 48(2003), No. 28, p.

4197.

[36] S.J. Lee and L.H.T. Do, Effects of copper additive on micro-arc oxidation coating of LZ91 magnesium-lithium alloy, *Surf. Coat. Technol.*, 307(2016), p. 781.

[37] X.M. Zhang, G.S. Wu, X. Peng, L.M. Li, H.Q. Feng, B. Gao, K.F. Huo, and P.K. Chu, Mitigation of corrosion on magnesium alloy by predesigned surface corrosion, *Sci. Rep.*, 5(2015), art. No. 17399.

[38] A.L. Yerokhin, L.O. Snizhko, N.L. Gurevina, A. Leyland, A. Pilkington, and A. Matthews, Spatial characteristics of discharge phenomena in plasma electrolytic oxidation of aluminium alloy, *Surf. Coat. Technol.*, 177-178(2004), p. 779.

[39] E. Mortezanejad, M. Atapour, H. Salimijazi, A. Alhaji, and A. Hakimizad, Wear and corrosion behavior of aluminate- and phosphate-based plasma electrolytic oxidation coatings with polytetrafluoroethylene nanoparticles on AZ80 Mg alloy, *J. Mater. Eng. Perform.*, 30(2021), No. 6, p. 4030.

[40] L. Prince, M.A. Rousseau, X. Noirfalise, L. Dangreau, L.B. Coelho, and M.G. Olivier, Inhibitive effect of sodium carbonate on corrosion of AZ31 magnesium alloy in NaCl solution, *Corros. Sci.*, 179(2021), art. No. 109131.

[41] L.F. Hou, M. Raveggi, X.B. Chen, W.Q. Xu, K.J. Laws, Y.H. Wei, M. Ferry, and N. Birbilis, Investigating the passivity and dissolution of a corrosion resistant Mg–33at.%Li alloy in aqueous chloride using online ICP-MS, *J. Electrochem. Soc.*, 163(2016), No. 6, p. C324.